Infinite Science
Publishing

Proceedings Article

An analytical equilibrium solution to the Néel relaxation Fokker-Planck equation

Marco Maass [a,*]· Christine Droigk [a]· Mathias Eulers [a]· Alfred Mertins [a,b]

[a]Institute for Signal Processing, University of Lübeck, Lübeck, Germany
[b]German Research Center for Artificial Intelligence (DFKI), AI in Biomedical Signal Processing, Lübeck, Germany
*Corresponding author, email: marco.maass@uni-luebeck.de

Abstract

In this work, an analytical equilibrium solution to the Néel relaxation Fokker-Planck equation with a uniaxial anisotropy is presented. The solution is compared with a recently developed mathematical model that explains the spatial structure of the system function better than the Langevin function based model. The results presented show small relative errors on a large scale of typical particle parameters, so that both models can be considered approximately equivalent. The parameter choice for which both models diverge is outlined. The advantage of the proposed solution is its fast calculation in contrast to the numerical solution of the Fokker-Planck equation.

I. Introduction

Magnetic particle imaging (MPI) is a tracer-based preclinical medical imaging method that measures the spatial distribution and concentration of superparamagnetic iron oxide nanoparticles (SPIOs) within a field of view (FOV). The imaging principle is based on the nonlinear magnetization behavior of SPIOs. Due to the lack of mathematical models in MPI, the standard procedure for MPI with Lissajous excitation is to measure the system function [1]. Nevertheless, various mathematical models have been developed to derive the system function [2]. The simplest model neglects particle anisotropies and relaxation effects and does not provide satisfactory image reconstruction results for higher dimensional excitation. If one wants to use more complex models the relaxation effects have to be modeled. Two types of relaxation effects in the SPIO distribution are typically prevalent: Brownian rotation, which describes the physical rotation of an SPIO when an external magnetic field is changed, and the Néel relaxation (NR), which models the relaxation of the SPIO's magnetic moment and allows the introduction of anisotropies. For the relaxation

effects, the magnetization behavior of SPIOs is described by stochastic differential equations (Langevin equations) or by partial differential equations (PDEs) (Fokker-Planck equations (FPEs)). The FPEs describe the probability density function (PDF) of the mean magnetic moment (MMM) of the SPIO distribution. Unfortunately, there are no analytical solutions for the typical MPI-FPEs and one has to solve the PDEs numerically. In a recent work, it is shown that the MMM derived from the FPE for NR better describes the spatial structure of a measured MPI system matrix when assuming a uniaxial easy axis (UAE) in the SPIOs and the easy axis is coincident with the direction of the static selection field [3]. Since the model B3 in [3] is computationally expensive, the authors themselves have concluded that additional simplifications to the model are required. A straightforward simplification is to assume that the magnetic fields in the FPE are static and the SPIOs have sufficient time to reach thermodynamic equilibrium. Since space is quite limited in this work, we compare this type of simplification only numerically with model B3 from [3] without giving many details of the derivation of the analytical solutions.

Table 1: The physical parameters in the simulated models.

	symbol	value	unit
Magnetic constant	μ_0	$4\pi \times 10^{-7}$	$\mathrm{H\,m^{-1}}$
Boltzmann constant	k_B	$1.38064852 \times 10^{-23}$	$\mathrm{J\,K^{-1}}$
Particle diameter	D	$\{20, 25, 30\} \times 10^{-9}$	m
Particle volume	V_C	$\frac{\pi}{6} D^3$	$\mathrm{m^3}$
Particle temperature	T_B	300	K
Sat. magnetization	M_S	474000	$\mathrm{J\,m^{-3}\,T^{-1}}$
Magnetic anisotropy	K_{anis}	$\{625, 1250, 2500\}$	$\mathrm{J\,m^{-3}}$
Gyromagnetic ratio	γ	1.75×10^{11}	$\mathrm{rad\,s^{-1}\,T^{-1}}$
Damping parameter	α	0.1	unitless
Relaxation time	τ_N	$\frac{V_C M_S (1+\alpha^2)}{2\alpha\gamma k_B T_B}$	s
	α_K	$\frac{V_C K_{\mathrm{anis}}}{k_B T_B}$	unitless
	β	$\frac{\mu_0 V_C M_S}{k_B T_B}$	$\mathrm{mA^{-1}}$

II. Methods and materials

The FPE for SPIOs with NR and a UAE is [2, Eq. (19)]

$$\frac{\partial p_N}{\partial t} = -\frac{1}{2\tau_N}\,\mathrm{div}_{\mathbb{S}^2}\left(\frac{\beta}{\alpha}\left(H_{\mathrm{eff}} \times m + \alpha(m \times H_{\mathrm{eff}}) \times m\right)p_N - \nabla_{\mathbb{S}^2} p_N\right) \quad (1)$$

and $H_{\mathrm{eff}} = H + 2\frac{\alpha_K}{\beta} n m^T n$ with $p_N(m, H, n)$ ($p_N : \mathbb{S}^2 \times \mathbb{R} \times \mathbb{S}^2 \to \mathbb{R}_+$) denoting the PDF. The operators $\nabla_{\mathbb{S}^2}$ and $\mathrm{div}_{\mathbb{S}^2}$ denote the gradient and divergence operators with respect to the surface of the unit sphere $\mathbb{S}^2 \subset \mathbb{R}^3$. It should be mentioned that in (1) a notation that is slightly different to the one in [2, Eq. (19)] is used. The physical parameters are defined in Table 1. The vector $m \in \mathbb{S}^2$ denotes a point on $\mathbb{S}^2$. The applied magnetic field $H : \mathbb{R}^3 \times \mathbb{R} \to \mathbb{R}^3$ is temporally and spatially changing and the UAE $n : \mathbb{R}^3 \to \mathbb{S}^2$ of the SPIOs is modeled as a vector on $\mathbb{S}^2$ depending on the applied magnetic field. For simplicity, (1) discards all parameters of the functions in the PDE. The MMM is given by

$$\bar{m}(H, n) = M_S V_C \int_{\mathbb{S}^2} m\, p_N(m, H, n)\,\mathrm{d}m, \quad (2)$$

whose temporal derivative is proportional to the system function $s(x, t)$ in MPI: $s(x, t) \sim \frac{\partial}{\partial t} \bar{m}(H, n)$.

Assuming that the system in (1) is in thermodynamic equilibrium ($\frac{\partial p_N}{\partial t} = 0$) then the solution is

$$p_N(m, H, n) = \frac{1}{\mathscr{Z}} e^{\beta H^T m + \alpha_K (n^T m)^2} \quad (3)$$

with the partition function (PF) $\mathscr{Z}$. The eq. (3) can be derived from [2, Appx. C], since the PDF p_N needs to fulfill $\nabla_m p_N = \beta H_{\mathrm{eff}} p_N$. It is worth noting that $\frac{\partial p_N}{\partial t} = 0$ is never satisfied for time-varying magnetic fields. A compact expression for the analytical solution of $\mathscr{Z}$ is sought. The PF can be written as

$$\mathscr{Z}(H, n) = \int_{\mathbb{S}^2} e^{\beta H^T m + \alpha_K (n^T m)^2}\,\mathrm{d}m = \int_{\mathbb{S}^2} e^{\beta (R_n H)^T m + \alpha_K m_3^2}\,\mathrm{d}m, \quad (4)$$

using for the second integral that $e_3 = R_n n$ with the rotation matrix R_n, e_3 denotes the third Cartesian unit vector, and the integral over $\mathbb{S}^2$ is rotationally invariant. Eq. (4) can also be represented as a 2D integral in spherical coordinates. We have succeeded in representing (4) as an

analytical 1D integral or as a single series expression, but due to the page limitations the derivation is omitted here. Using the auxiliary variable $H = R_n^T \tilde{H}$, the MMM $\bar{m}_n : \mathbb{R}^3 \to \mathbb{R}^3$ in the rotated coordinate system is given by $\bar{m}_n(\tilde{H}) = \frac{M_S V_C}{\mathscr{Z}} z(\tilde{H})$, where the PF and the vector components of z are given by

$$\mathscr{Z}(R_n^T \tilde{H}, n) = 2\pi \int_{-1}^{1} I_0\left(\beta|\tilde{H}|_{12}\sqrt{1-x^2}\right) e^{\beta\tilde{H}_3 x + \alpha_K x^2}\,\mathrm{d}x$$

$$z_3(\tilde{H}) = 2\pi \int_{-1}^{1} x\, I_0\left(\beta|\tilde{H}|_{12}\sqrt{1-x^2}\right) e^{\beta\tilde{H}_3 x + \alpha_K x^2}\,\mathrm{d}x$$

$$z_j(\tilde{H}) = 2\pi \frac{\tilde{H}_j}{|\tilde{H}|_{12}} \int_{-1}^{1} \sqrt{1-x^2} I_1\left(\beta|\tilde{H}|_{12}\sqrt{1-x^2}\right) e^{\beta\tilde{H}_3 x + \alpha_K x^2}\,\mathrm{d}x, \quad (5)$$

where $|\tilde{H}|_{12} = \sqrt{\tilde{H}_1^2 + \tilde{H}_2^2}$, $I_a(\xi)$ denotes the modified Bessel function of the first kind with order $a \in \mathbb{R}$, and $j \in \{1, 2\}$. If we represent the term $e^{\beta\tilde{H}_3 x + \alpha_K x^2}$ by a Taylor series and resolve the integrals in (5), we obtain

$$\mathscr{Z}(R_n^T \tilde{H}) = (2\pi)^{\frac{3}{2}} \sum_{\ell=0}^{\infty} (2\alpha_K)^\ell L_\ell^{(-\frac{1}{2})}\left(-\frac{\beta^2 \tilde{H}_3^2}{4\alpha_K}\right) \frac{I_{\frac{1}{2}+\ell}(\beta|\tilde{H}|_{12})}{(\beta|\tilde{H}|_{12})^{\frac{1}{2}+\ell}},$$

$$z_3(\tilde{H}) = (2\pi)^{\frac{3}{2}} \beta\tilde{H}_3 \sum_{\ell=0}^{\infty} (2\alpha_K)^\ell L_\ell^{(\frac{1}{2})}\left(-\frac{\beta^2 \tilde{H}_3^2}{4\alpha_K}\right) \frac{I_{\frac{3}{2}+\ell}(\beta|\tilde{H}|_{12})}{(\beta|\tilde{H}|_{12})^{\frac{3}{2}+\ell}}, \quad (6)$$

$$z_j(\tilde{H}) = (2\pi)^{\frac{3}{2}} \beta\tilde{H}_i \sum_{\ell=0}^{\infty} (2\alpha_K)^\ell L_\ell^{(-\frac{1}{2})}\left(-\frac{\beta^2 \tilde{H}_3^2}{4\alpha_K}\right) \frac{I_{\frac{3}{2}+\ell}(\beta|\tilde{H}|_{12})}{(\beta|\tilde{H}|_{12})^{\frac{3}{2}+\ell}},$$

where $L_n^{(a)}(\xi)$ denotes the generalized Laguerre polynomials with $a > -1$ and degree $n \in \mathbb{N}_0$. Note that the solution of the MMM collapses into the classical solution of the Langevin function when $\alpha_K \to 0$. Finally, the MMM in the original coordinate system is obtained by $\bar{m}(H, n) = R_n^T \bar{m}_n(R_n H)$.

III. Experiments

The scanner-dependent parameters were chosen according to the 2D Lissajous sequence from the dataset in [4]. The FOV is over-scanned symmetrically to $37\,\mathrm{mm} \times 37\,\mathrm{mm}$ and finally equidistantly sampled on a grid of 37×37 positions x_n ($n \in \{0, 1, \dots, 1368\}$). A temporal period of the signal is uniformly sampled to 3000 points.

The proposed model B3 in [3] is used, where the easy axis $n(x) = \frac{H_S(x)}{\|H_S(x)\|}$ is aligned with the selection field and the anisotropy constant is spatially varying by $K_{\mathrm{anis}}(x) = g_{K_{\mathrm{anis}}} \frac{\|H_S(x)\|_2}{\max_{x \in \Omega}\{\|H_S(x)\|_2\}}$, where $g_{K_{\mathrm{anis}}}$ is the anisotropy gradient and Ω is the drive-field FOV. In the experiments, the particle diameters $D \in \{20\,\mathrm{nm}, 25\,\mathrm{nm}, 30\,\mathrm{nm}\}$ and gradients $g_{K_{\mathrm{anis}}} \in \{625\,\mathrm{J\,m^{-3}}, 1250\,\mathrm{J\,m^{-3}}, 2500\,\mathrm{J\,m^{-3}}\}$ were varied.

For comparison, the FPE in (1) is solved numerically for each of the 37×37 positions using the toolbox provided by [5] and within the toolbox using the spherical harmonic method. To ensure that a steady state of the simulated system is achieved, three periods of the signal were simulated and the last period was used. The equilibrium solutions were derived by truncation of the series
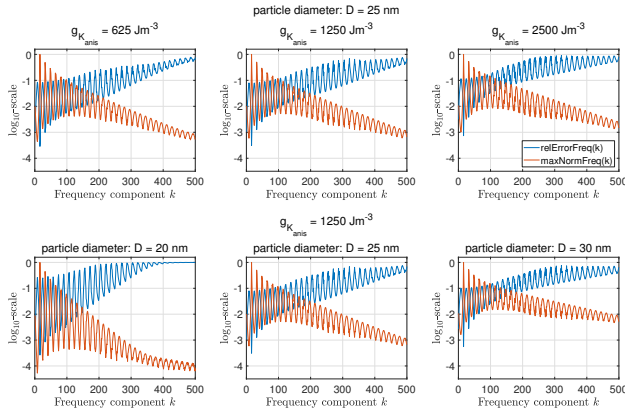
Figure 1: Relative approximation error (blue) and maximal norm of system function components (red) for the x-coil as function over the frequency index k.

in (6). Then, all solutions were derivated numerically in time, and subsequently the frequency components k of the system functions were obtained by a discrete-time Fourier transform. The FPE solution is denoted by $s_k^{\mathrm{FP}}(\boldsymbol{x}_n)$, while the equilibrium solution is $s_k^{\mathrm{EQ}}(\boldsymbol{x}_n)$.

The relative approximation errors and maximal norms of the system function components between the numerical solution of the FPE and the equilibrium solution are calculated as follows

$$\mathrm{relErrorFreq}(k) = \sqrt{\frac{\sum_{n=0}^{1368} |s_k^{\mathrm{FP}}(\boldsymbol{x}_n) - s_k^{\mathrm{EQ}}(\boldsymbol{x}_n)|^2}{\mathrm{maxEngFreq(k)}}}$$

$$\mathrm{maxEngFreq}(k) = \max\left\{\sum_{n=0}^{1368}|s_k^{\mathrm{FP}}(\boldsymbol{x}_n)|^2, \sum_{n=0}^{1368}|s_k^{\mathrm{EQ}}(\boldsymbol{x}_n)|^2\right\} \quad (7)$$

$$\mathrm{maxNormFreq}(k) = \sqrt{\frac{\mathrm{maxEngFreq}(k)}{\max_k\{\mathrm{maxEngFreq}(k)\}}}.$$

IV. Results and discussion

In Figure 1, one can see that the relative approximation error of a frequency component for the x-coil is low when the norm of a system function component is high and vice versa. The upper row shows that the approximation error increases over the frequencies with an increasing anisotropy gradient $g_{K_{\mathrm{anis}}}$. The bottom row shows that as the diameter D increases, the norm of the system function component decreases more slowly for larger frequency indices k. The results for the y-coil are not shown, but behave similar.

The results are not surprising, since it could be expected that with increasing anisotropy K_{anis} or increasing particle diameter D, the importance of the Néel relaxation time τ_{N} would become more dominant and therefore the two models would differ more. On the one hand, the relative approximation error for frequency components is high when their norm is low (see Figure 1). On the other hand, such components are usually discarded when selecting frequency components for image

reconstruction because they usually have a poor signal-to-noise ratio. It should not go unmentioned that the numerical solving of the FPE (1) has by itself an approximation error against the unknown ground truth solution. The behavior in Figure 1 for large $k > 300$, $D = 20\,\mathrm{nm}$, and $g_{K_{\mathrm{anis}}} = 1250\,\mathrm{J\,m^{-3}}$ can be directly attributed to this, since the norm of the system function component is quite low and within the range of the relative tolerance of the ODE-solver. Although the new equilibrium model is not a general solution for all conceivable parameter settings for the FPE in (1), it appears to be in high agreement when the particle diameter is smaller than $30\,\mathrm{nm}$ and its anisotropy gradient is smaller than $2500\,\mathrm{J\,m^{-3}}$. Also according to [3] an anisotropy gradient of $1250\,\mathrm{J\,m^{-3}}$ seems to be a realistic parameter. However, an exhaustive investigation must be performed in the future. The main advantage of the proposed model is that it can be computed much faster than the numerical solution of the FPE. For instance, the solution for the FPE on twelve parallel workers takes about ten days for the setting $D = 30\,\mathrm{nm}$ and $g_{K_{\mathrm{Anis}}} = 1250\,\mathrm{J\,m^{-3}}$, while the same setting with the truncated series in (6) with 241 terms takes only 684 s on a single worker on the same server.

V. Conclusion

In this work, the Néel relaxation FPE and a corresponding equilibrium model were used to obtain an analytical solution in (6) for the mean magnetic moment in (2) and the partition function in (4). The model allows for a comparison with the recently introduced and improved mathematical model for the system function in [3]. This publication indicates that the proposed model is in high agreement with the recently published work. Although not demonstrated here, it seems realistic for the first time to derive a three-dimensional system function using the spatial model of [3], which could not be obtained before in a reasonable time. Upcoming publications will show the exact mathematical derivation of the model and investigate its suitability for image reconstruction in two- and three-dimensional MPI cases.

Author's statement

Authors state no conflict of interest.

References

[1] T. Knopp and T. M. Buzug, Magnetic Particle Imaging: An Introduction to Imaging Principles and Scanner Instrumentation. Berlin/Heidelberg: Springer, 2012, doi:10.1007/978-3-642-04199-0.

[2] T. Kluth. Mathematical models for magnetic particle imaging. *Inverse Problems*, 34(8):083001, 2018, doi:10.1088/1361-6420/aac535.

[3] T. Kluth, P. Szwargulski, and T. Knopp. Towards accurate modeling of the multidimensional magnetic particle imaging physics. *New J. Phys.*, 21(10):103032, 2019, doi:10.1088/1367-2630/ab4938.

[4] T. Knopp, P. Szwargulski, F. Griese, and M. Gräser. OpenMPIData: An initiative for freely accessible magnetic particle imaging data. *Data in Brief*, 28:104971, 2020, doi:10.1016/j.dib.2019.104971.

[5] H. Albers, T. Kluth, and T. Knopp. MNPDynamics: A computational toolbox for simulating magnetic moment behavior of ensembles of nanoparticles. *Int. J. Mag. Part. Imag.*, 6(2):2009020, 2020, doi:10.18416/IJMPI.2020.2009020.